Proceedings of the
Annual Stability Conference
Structural Stability Research Council
Charlotte, North Carolina, April 11-14, 2023

Experimental and numerical investigation of the impact of non-uniform end bearing conditions on the axial capacity of global height, unsheathed, cold-formed steel wall assemblies

Divyansh R. Kapoor[1], Hernan Castaneda[2], Abbas Joorabchian[3], Zhanjie Li[4], Kara D. Peterman[5]

Abstract

Cold-formed steel load-bearing walls are commonly installed on concrete slab floors. While these floors may appear sufficiently rigid, they impart a non-uniform bearing condition on the ends of the stud walls. This non-uniformity can be caused by surface roughness, or the distance to the edge of the slab. Some wall assemblies are even erroneously installed overhanging from the slab edge. The impact of these non-uniform end bearing conditions on the axial capacity of unsheathed, variable height, cold-formed steel stud-track wall assemblies was investigated via a suite of 58 experimental tests and 1716 high-fidelity finite element models. While the assembly heights were varied to assess performance at heights corresponding to local, distortional, and global half-wavelengths, only the global effort is presented herein. The test specimens were comprised of 600S162 cold-formed steel structural sections (C-studs), that varied in thickness, and end bearing condition. Bearing conditions were parametrically varied from full-bearing (i.e., middle of slab) to 0.50 in (25.4 mm) overhang. Results from the experimental investigation were utilized to develop and calibrate high-fidelity finite element models. These models utilized imperfections, contact definitions, non-linear material properties, and were used to expand the investigation to 12 cross sections and 7 unique bearing conditions presented in this paper. The selected cross-sections varied in stud depth, flange width, lip width, and thickness. Results from the experimental study and parametric evaluation are presented and compared with theoretical (Euler) and design (AISI S100 - Direct strength method) equations to assess the performance of predictive methods and evaluate the impact of varying bearing conditions.

1. Introduction and background

The behavior of cold-formed steel axial members has been investigated comprehensively and implemented for design and construction in the American Iron and Steel Institute (AISI) specifications. Axial members are governed by the provisions of AISI S100-16 (AISI 2016) and AISI S240-15 (AISI 2015). In these provisions, a uniform stress distribution is assumed to exist at the stud ends but this condition is not necessarily realistic. Load-bearing walls are typically placed on concrete slab floors. Exterior walls may be installed at or near the slab edge or may even

[1] Graduate Research Assistant, University of Massachusetts, Amherst, MA, dkapoor@umass.edu
[2] Consulting Engineer, Simpson Gumpertz and Heger, Waltham, MA, hcastaneda@umass.edu
[3] Senior Structural Engineer, Thornton Tomasetti, Boston, MA, ajoorabchian@umass.edu
[4] Associate Professor, SUNY Polytechnic Institute, Utica, NY, zhanjie.li@sunypoly.edu
[5] Associate Professor, University of Massachusetts, Amherst, MA kdpeterman@umass.edu

overhang slightly due to erroneous installation. These conditions may result in a non-uniform bearing condition and stress distribution at the stud ends. Studs bearing under these situations can have reduced axial capacity, yet current practice does not recognize a difference in the axial capacity or behavior due to partial end supports caused by edge distance, overhang, or non-uniform bearing surface.

Polyzois and Fox (2011) investigated stud capacities on concrete slabs. The experimental program included stud-track assemblies located 8 in., 1 in. from, and at the concrete slab edge. The studs were sized to buckle locally. They found that assemblies located 8.0 in. from the slab edge developed their local buckling capacity. However, assemblies installed at the edge were hindered by concrete spalling and cracking, and axial capacity decreased by 15%–25%. This decrease was due to the reduction in bearing area and loss of uniform stress distribution at the ends. This work only examined one stud-track assembly and did not consider intermediate edge distances. Bae et al. (2006) examined stub stud walls bearing on slabs. Different configurations of the stud-track assembly were tested on a 3.5 in. concrete slab. The studs were 2 in. long to force failure into the slab. Finite element analysis (FEA) was conducted to determine the stress distribution in the concrete slab through the track section. The work demonstrated that edge distance did impact system bearing strength, and results were used to develop a method of determining the bearing area for the stud-track assembly on concrete slabs. While this study expanded the state of knowledge for how stud assemblies interact with concrete foundations, it was limited in scope to one stud size and one stud height, and the short stub column height did not permit buckling of the stud.

Joorabchian et al. (2021) performed extensive numerical and experimental investigation on the influence of non-uniform bearing conditions on the axial capacity of members. The study considered specimen at the local, distortional, and global heights and 58 experimental tests were performed to quantify the impact. The experimental study was expanded to 66 cross sections and 13 bearing conditions via a suite of 1872 calibrated finite element models with specimen heights corresponding to their local and distortional wavelengths. This paper expands upon these previous works by expanding the numerical study to 12 cross sections and 7 bearing conditions (84 new configurations) at the global height. Results from the 12 global height experiments are used to calibrate FEA models (Fig. 1) which are then used to predict capacity. The FEA modelling methodology, validation, expansion to untested configurations, and performance of predictive methods are presented in this paper.

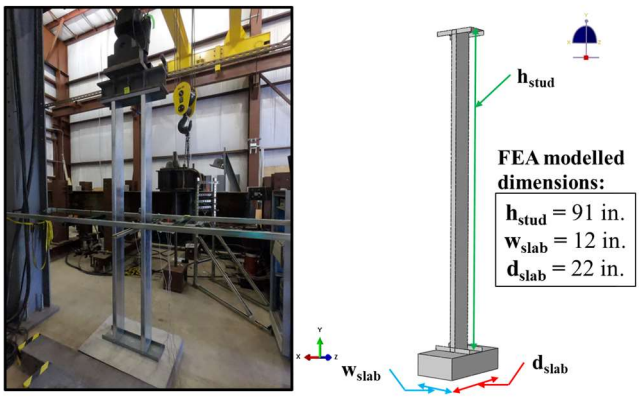

Figure 1: Experimental specimen and finite element analysis idealization

2. Experimental results

To evaluate the impact of non-uniform end bearing conditions on the axial capacity of global height, unsheathed, cold-formed steel wall assemblies, twelve 91 in. tall specimen were experimentally tested at the Robert B. Brack Structural Testing Facility at UMass, Amherst. The 600S162 cross section was evaluated with three thicknesses (33 mil, 54 mil, and 97 mil) at four bearing conditions [Full bearing (FB), 0.5 in. to the edge (E0.5), at the edge (E0.0), and 0.5 in. overhang (OH0.5)]. The force-displacement response and comparison of capacity observed at bearing conditions (P_i) with capacities in the full bearing (P_{FB}) case can be seen in Figure 2 and Figure 3 below. Here the dashed grey lines are the expected AISI S100 (AISI 2016) capacities.

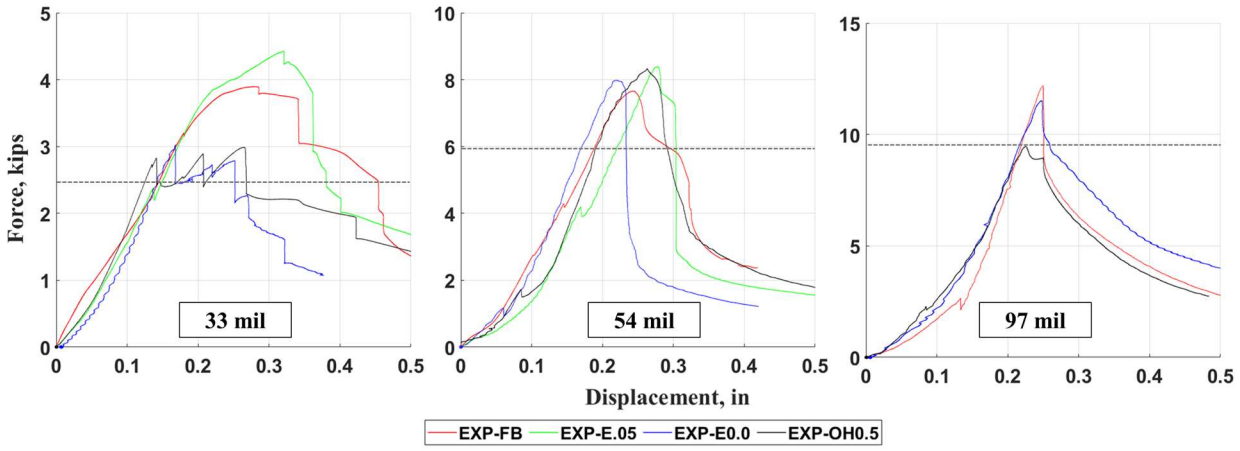

Figure 2: Force-displacement results of the tested 600S162 cross section specimen

Both the 33 mil and 97 mil overhanging specimens suffered significant capacity losses due to the combined effect of the reduced stud section (smaller bearing area) and the induced eccentricity resulting in bending moment on the stud. This reduction was on average 0.23. No reduction in capacity was observed in the overhanging 54 mil specimen. A reduction was also observed in assemblies located at the edge (mean reduction 0.08) similar to the local and distortional height specimen (Joorabchian et al. 2021, Joorabchian 2021) and this was attributed to end condition sensitivity of the studs to localized geometric variation in the concrete slabs. Additionally, a change in buckled shape was observed in all the specimen as they moved over the edge except for the 54-mil specimen.

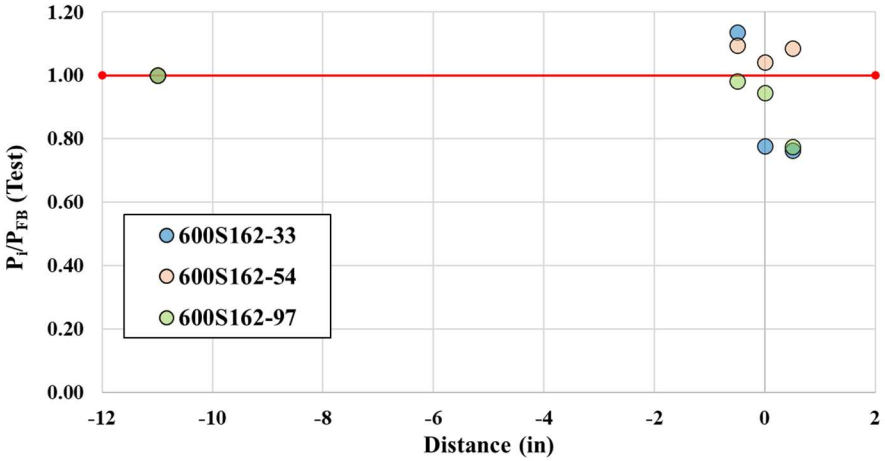

Figure 3: Observed reduction in capacity in experimental tests

3. Development of finite element model

To expand the available test data to untested configurations, a finite element modelling methodology with non-linear material properties, non-linear geometry, and idealized boundary conditions was developed. The objective of developing this methodology was to establish a uniform set of parameters which could be applied homogenously to a suite of commercially available CFS cross sections. The models were calibrated to the 12 global height experimental tests discussed in Section 3. Each model was evaluated at the 4 boundary conditions (Fig. 4) evaluated during experimental testing. The following subsections outline the assumptions used to model the experimental specimen in ABAQUS and their validation with experimental data.

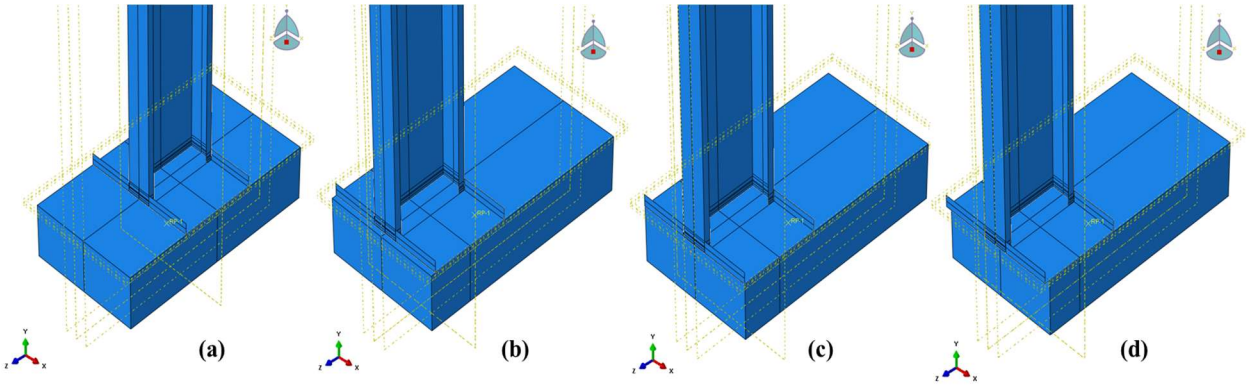

Figure 4: Modelled bearing conditions:
(a) Full bearing [FB] (b) 0.5 in. to edge [E0.5] (c) At edge [E00] (d) 0.5 in overhang [OH0.5]

3.1 Model geometry and material properties

The cold-formed steel (CFS) stud and track cross sections were modelled with sharp corners, nominal dimensions (SSMA 2022), and measured material properties and thicknesses from 9 ASTM E8 (ASTM 2016) compliant coupon tests. Three coupons were taken for each of the tested thickness from stud webs in the middle and ends of the section. These coupons were tested in a 11.25-kip Instron universal testing machine and complete details of the test results, testing procedure, and setup can be found in Joorabchian et al. (2021) and Joorabchian (2021). The modulus of elasticity (E) and Poisson's ratio (v) were assumed to be 29,500 ksi and 0.3 respectively. Average results (Fig. 5) from coupon tests for each of the thickness were converted from engineering stress and strain [Fig. 5.(a)] to true stress and plastic strain [Fig. 5.(b)] to account for material plasticity in Abaqus (ABAQUS 201).

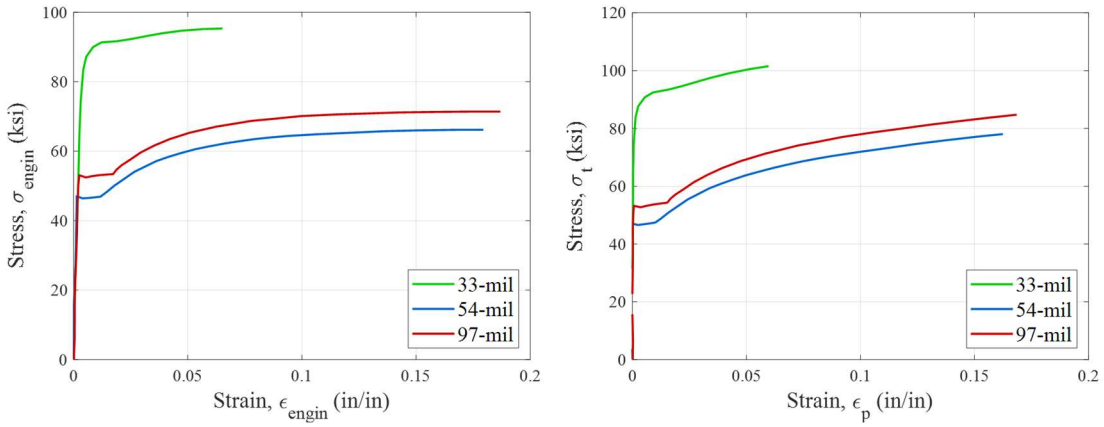

Figure 5: Material properties: (a) ASTM E8 coupon tests (b) Abaqus idealization

Concrete tensile and compressive properties for modelling were estimated from 18 cylinder tensile and compressive tests. These cylinders were cast in compliance with ASTM C31M-18b (ASTM 2018.a) during the casting of the concrete slabs used in the experimental program. Testing was done in a FX500 Forney machine and complete test results, testing procedure, and setup can be found in Joorabchian et al. (2021) and Joorabchian (2021). The average cylinder failure stress in compression (f'_c) and tension (f'_t) was found to be 4.81 ksi and 0.34 ksi respectively. The Poisson's ratio was assumed to be 0.18 (Joorabchian 2021). Concrete compressive behavior for the models was captured using a Hognestad Parabola (Fig. 6).

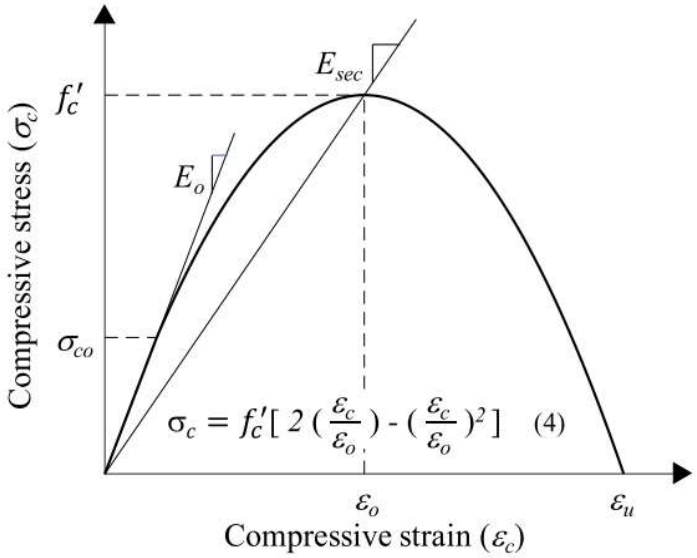

Figure 6: Uniaxial compressive stress strain curve for concrete [Adapted from Genikomsou and Polak (2015)]

Here, the compressive behavior of concrete is split into three regions, a linear elastic region with modulus of elasticity E_o of $5500(f'c)^{0.5}$ until σ'_{co} (0.4 f'_c), followed by the Hognestad parabola to f'_c and then failure. Figure 7 below represents the tensile stress - crack width relation and resulting tensile stress – strain curve utilized to model the tensile behavior of concrete in the models. Here the tensile stress strain behavior post f'_t till ultimate strain was modelled with a bilinear stress strain curve. Complete description of determining the concrete model properties used for analysis can be found in Joorabchian (2021).

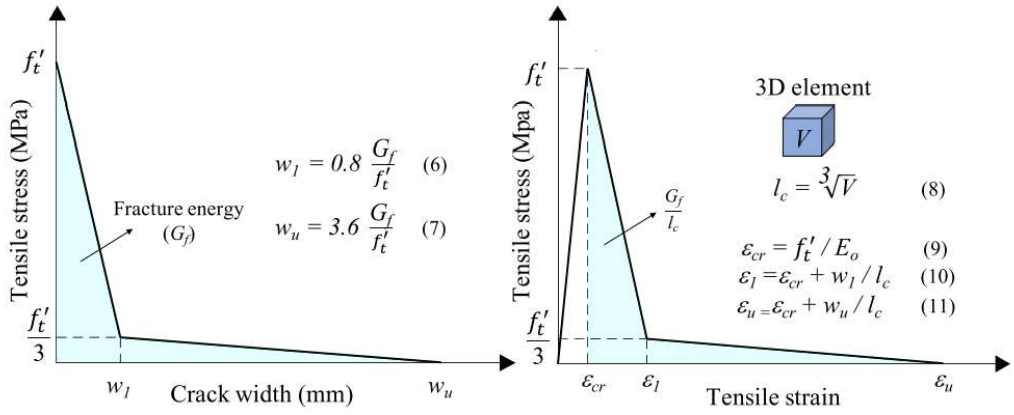

Figure 7: Concrete tensile cracking and stress strain behavior [Adapted from Joorabchian et al. (2021)]

3.2 Interactions and constraints

To apply load concentrically through the center of gravity (c.g.) of the specimen, reference points were located on the top track and bottom of the slab at the c.g. of the cross sections. These reference points were then tied to the top track web (Fig. 8) and bottom slab surface (Fig. 8) using the inbuilt Abaqus MPC beam constraints. Fasteners for connecting the stud and track flanges and the bottom track web to concrete slab were modelled with MPC beam constraints as well.

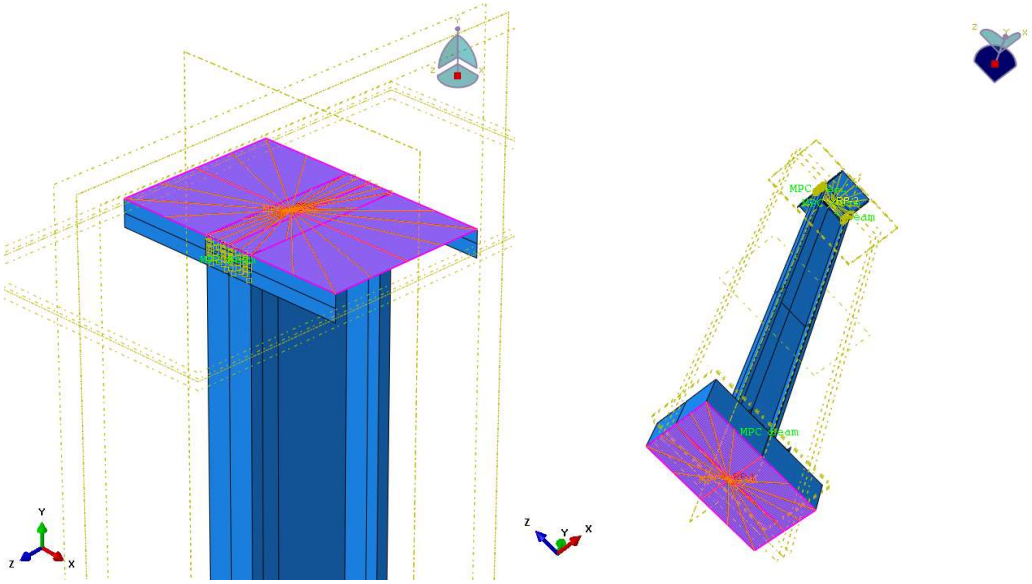

Figure 8: MPC beam constraints at specimen ends

To simulate load-transfer through bearing in the model, contacts were defined between the CFS stud ends and CFS track webs [Figure 9.(a)] and CFS track webs and top of the concrete slab [Figure 9.(c)]. These contacts were modelled with small sliding, Abaqus default hard contact in the normal direction, and frictionless behavior in the tangential direction. Contacts were also defined between the stud and track flanges [Figure 9.(b)] to simulate realistic warping restraint at stud ends in the model. These surface-to-surface contacts were modelled with finite sliding, default hard contact in the normal direction, and frictionless behavior in the tangential direction.

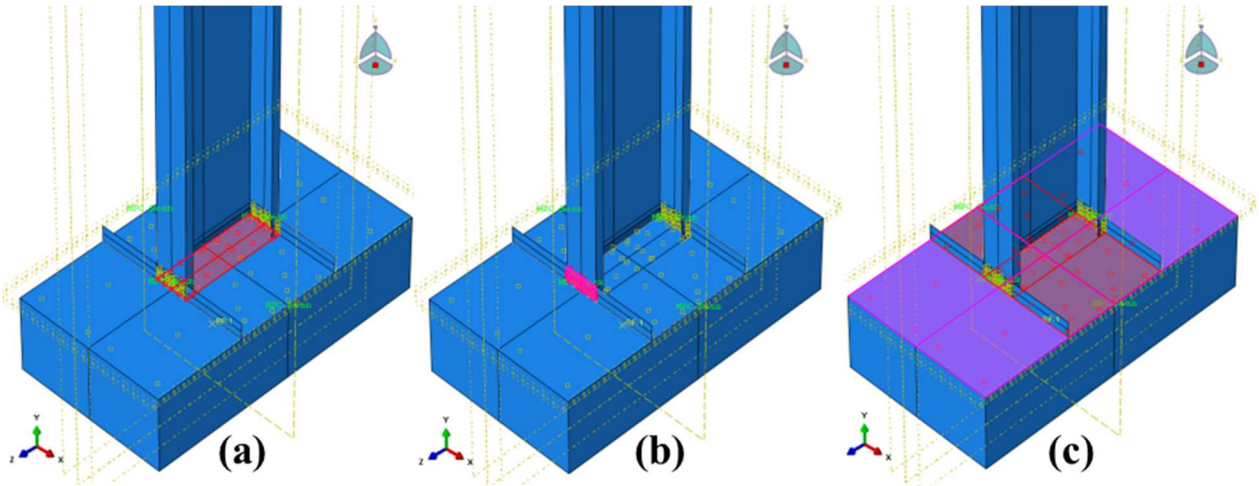

Figure 9: Contact definitions:
(a) Stud end and track web (b) Stud and track flange (c) Track web and concrete slab

3.3 Meshing details

A fine mesh (element size = 0.125 in) and a medium-course mesh (element size = 1.0 in) were utilized to discretize the CFS sections and concrete slab respectively (Fig. 10). The CFS sections were modelled with 4 node, reduced integration, S4R shell elements (ABAQUS 2014) with 9 integration points through the thickness. The selected mesh size ensured that even in the smallest cross section, at least 29, 11, and 3, elements were used to model the web, flange, and lip respectively. Further the mesh was partitioned to conveniently locate fasteners and contact regions. The concrete slab was modelled with 8 node, reduced integration, C3D8R solid elements (ABAQUS 2014) and had partitions for locating contact regions and fasteners.

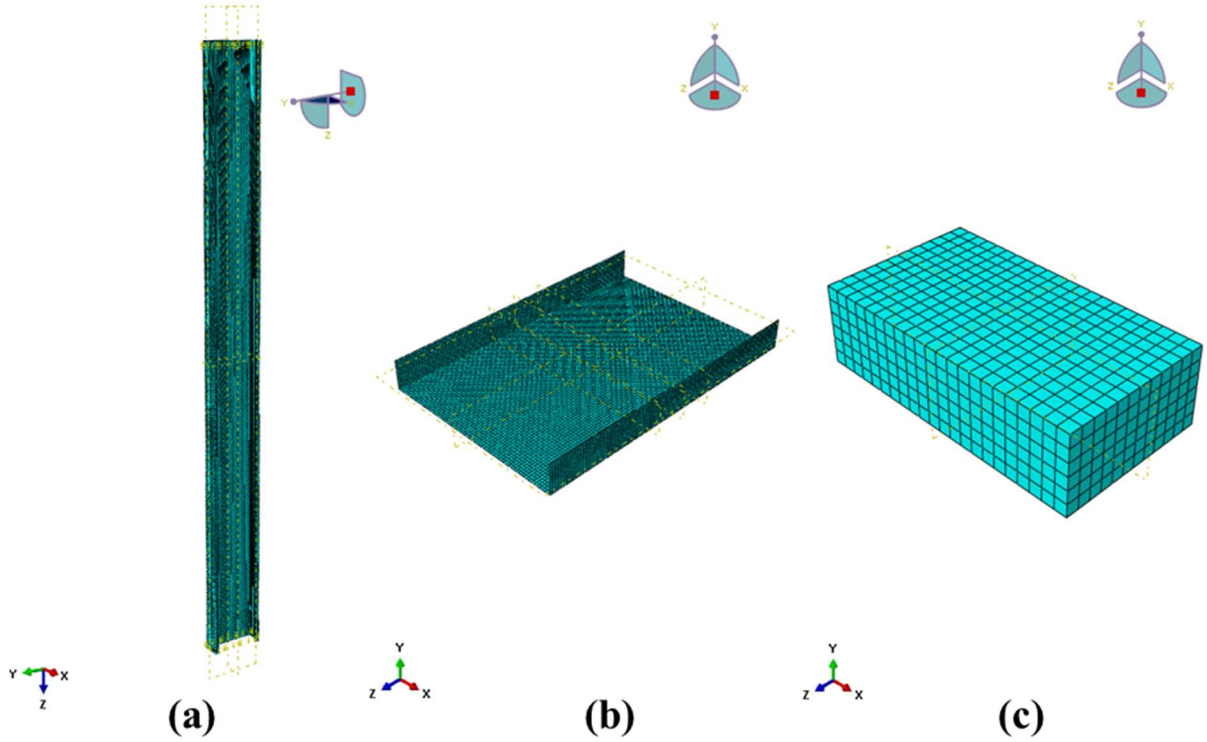

Figure 10: Part meshing (a) Stud (b) Track (c) Concrete Slab

3.4 Geometric imperfections

Imperfections were included in the collapse analysis for capturing failure modes observed in the experimental tests and to account for manufacturing defects caused due to cold rolling (Shafer et al. 2010). Imperfections impact capacity of CFS members and are essential for accurately estimating failure load. As the parametric analysis consisted of a large suite of CFS sections, direct measurements of imperfections were not possible, and mode shape-based imperfections were included through an elastic buckling analysis. This also ensured a homogenous modelling methodology across the models. Scaled flexural and flexural-torsional (Fig. 11) mode shapes were seeded into the FEA model based on literature recommended amplitudes. The selected amplitudes corresponded with 50% probability of exceedance as reported in Zeinoddini and Schafer (2011). This amplitude was also selected to be consistent with previous works completed and reported in Joorabchian et al. (2021).

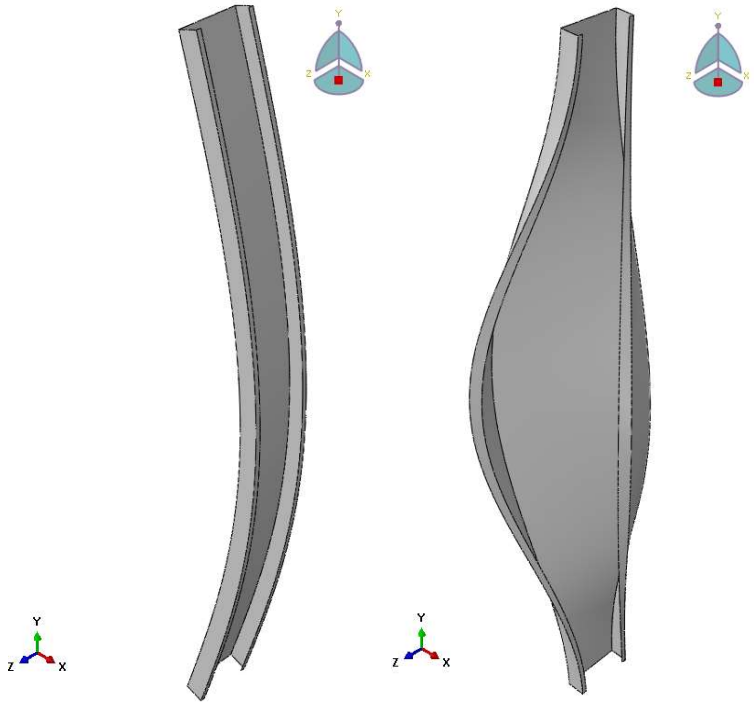

Figure 11: Abaqus flexural and flexural torsional generated imperfection shapes

3.5 Boundary conditions, applied displacement, and solver

The experimental results and buckled shapes indicated a simply supported end condition (Experimental effective length factor, K_{exp} = 0.97) and this was simulated in the model by restricting degrees of freedom of the reference points constraining the top track web and bottom slab surface. The top node was restricted in all translational and rotational degrees of freedom except for U2 and UR3 (U1 = U3 = UR1 = UR2 = 0). This allowed the top track to rotate as was observed in the experimental tests. The bottom reference point was restricted in all translational and rotational degrees of freedom except for UR3 (U1 = U2 = U3 = UR1 = UR2 = 0). Displacement was applied incrementally through the top reference point in the negative U2 direction.

A static general load step with default dissipated energy fraction (Joorabchian et al. 2021) was used to apply the displacement. The incrementation was conservatively reduced to an initial size of 0.0005 in./increment and maximum size of 0.005 in./increment. This resulted in all the models completing at least 20 increments before the onset of buckling and incrementation size could be kept constant across the experimental validation and parametric evaluation.

3.6 Gap measurements and treatment in FEA modelling

Gap closure affects the initial stiffness of the model as documented in Joorabchian et al. (2021) and gaps were measured with feeler gauges after seating at 12 locations for each specimen. The location of gap measurement and histogram of occurrence can be seen in Figure 12 below. This was also done to ensure that gaps in the experiments did not exceed recommendations in AISI S240 – 15 (2015). Although gaps paired with non-linear fastener models help with capturing initial stiffness in FEA models, gaps were excluded from the models as no gap measurement data existed for untested configurations. The impact of excluding gaps from the FEA models has been discussed in Section 3.7.

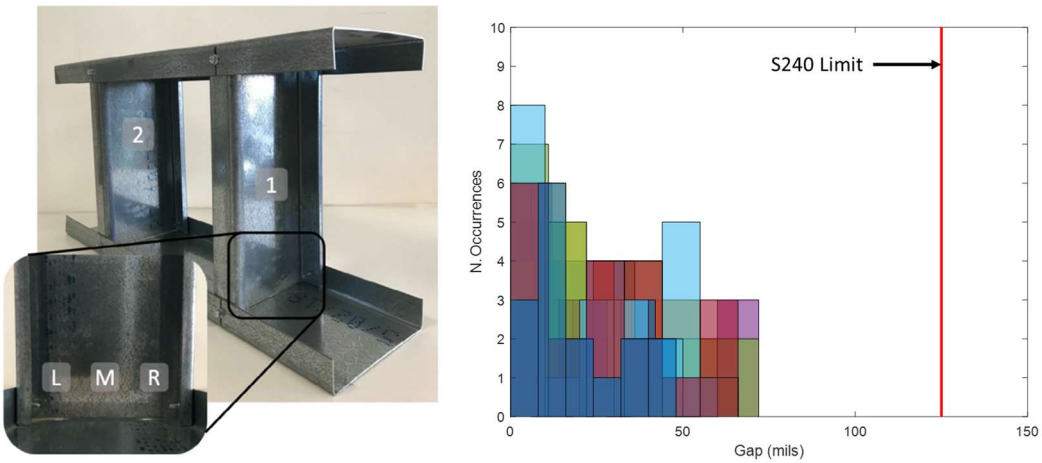

Figure 12: Measured gaps in global height specimen [reported in mils (1 mil = 1/1000 in)]

3.7 Comparison with experimental data

Figure 13, Figure 14, and Figure 15 below compare the force-displacement response, tested to model predicted capacities, and failure modes from the experimental tests with results from the FEA models. The homogenous modelling method and parameters defined in Section 4 were able to predict experimental capacities accurately (Fig. 13 and Fig. 14) with some exceptions (Mean test to predicted = 1.02, standard deviation = 0.14). There was good agreement with peak strength in the full bearing specimen (mean = 1.01, standard deviation = 0.01) but the reduction predicted by the FEA models was lower than that observed in the tests (Reduction test = 0.20 vs 0.14 from FEA). Additionally, the model predicted a reduction at the 600S162 – 54 mil OH05 case but no reduction was observed in the experiment at this bearing condition.

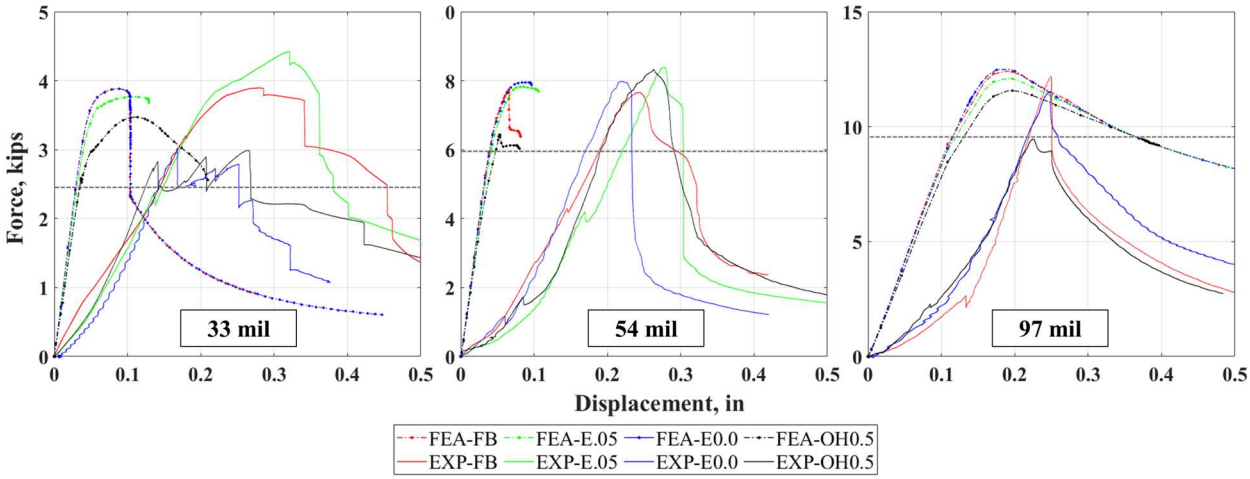

Figure 13: Comparison of tested and FEA model force-displacement response

The stiffness of the FEA models was also higher than experimental stiffness. This was found to be due to the default contact properties used in the normal direction to simulate the studs bearing on the track web. Switching to a penalty formulation where defining contact stiffness behavior is possible greatly improved the stiffness agreement but had its limitations. This method was found to be highly sensitive to mesh size and member gage and required calibration for each cross section, making it unsuitable for the planned parametric evaluation. The initial gap closure region

observed in the tests was also not captured by the models due to the exclusion of gaps and non-linear fastener data. However, since the exclusion of gaps did not impact capacity predictions and made the models more efficient in terms of runtime, gaps were not included in the modelling methodology.

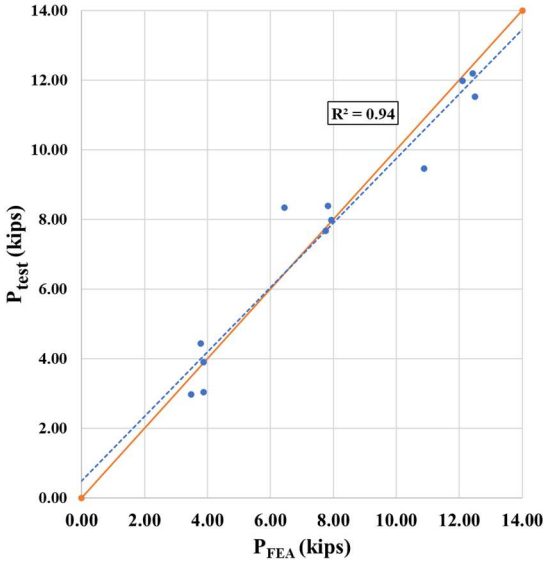

Figure 14: Comparison of tested axial capacity (P_{test}) and model predicted capacity (P_{FEA})

Figure 15 below compares buckled shapes observed in the 600S162 – 97 mil E0.0 and 600S162 – 54 mil FB assembly with FEA model predicted buckled shapes. Good agreement was found between the models and experiments and the models were capable of capturing the flexural and flexural-torsional buckled shapes observed during testing.

Figure 15: Comparison of failure modes: (a) 97 mil E0.0 (b) 54 mil FB

Although the FEA models did not replicate experimental results perfectly, the simplified modelling methodology developed was deemed suitable for the parametric evaluation to assess the reduction due to non-uniform bearing conditions. The homogenous modelling parameters such as idealized material properties, nominal cross sections, default constraints and contact properties, exclusion of gaps made it such that no section specific measured information or additional modeler intervention was required to complete the parametric study.

4. Parametric study

The FEA model developed and calibrated in Section 3 was used to expand available test data to 12 cross sections and 7 bearing conditions (84 unique configurations). The following subsections present the modelling matrix, material properties for the analysis, and summary results.

4.1 Modelling matrix

The numerical modelling matrix for FEA expansion can be seen in Table 1 below. The selected cross sections vary in web depth, flange width, thickness, bearing, condition, and grade of steel. All 43 and 54 mil specimen were modelled with bi-linear stress strain curves and yield strength, ultimate strength, and assumed elongation at failure have been reported in Table 1.

Table 1: FEA modelling matrix

Web depth	Flange width	Thicknesses	Bearing Condition
(in)	(in)	(mil)	(--)
3.625	1.375 & 1.625	43 & 54	FB, E2.0, E1.0, E0.5, E00, OH0.5, OH1.0
6.000	1.625 & 2.500	43 & 54	FB, E2.0, E1.0, E0.5, E00, OH0.5, OH1.0
8.000	1.625 & 2.500	43 & 54	FB, E2.0, E1.0, E0.5, E00, OH0.5, OH1.0

Notes:

- 3 web depths x 2 flange widths x 2 thicknesses x 7 bearing conditions = 84 configurations
- 43 mil – (F_y = 33 ksi, F_u = 52 ksi @ 18% elongation)
- 54 mil – (F_y = 50 ksi, F_u = 65 ksi @ 18% elongation)

4.2 Summary results

Capacities predicted by the FEA model for the 84 proposed configurations were compared to establish impact of non-uniform bearing conditions in the model. Predicted capacities at non-uniform bearing conditions (P_i) were compared with the predicted full-bearing capacities (P_{FB}) (Table 2 and Fig.16) to estimate P_i/P_{FB}. The FEA models predicted a reduction in capacity in the overhang cases (mean reduction OH0.5 = 0.20, mean reduction OH1.0 = 0.23). The standard deviation was also observed to increase in the 0.5 in. to edge and overhang assemblies (E0.5, E0.0, OH0.5, OH1.0) when compared to assemblies located 1 in. or further away from the edge (E1.00 & E2.00). A change in stress distribution at the ends was also observed in the OH0.5 and OH1.0 assemblies when compared to assemblies located at and further away from the edge.

Table 2: Mean capacity at bearing conditions w.r.t to full bearing [mean (P_i/P_{FB})]

	Bearing Condition						
	FB	**E2.0**	**E1.0**	**E0.5**	**E0.0**	**OH0.5**	**OH1.0**
Mean	1.00	1.01	0.99	0.93	1.00	0.80	0.77
St. Dev	0.00	0.02	0.04	0.08	0.07	0.12	0.09

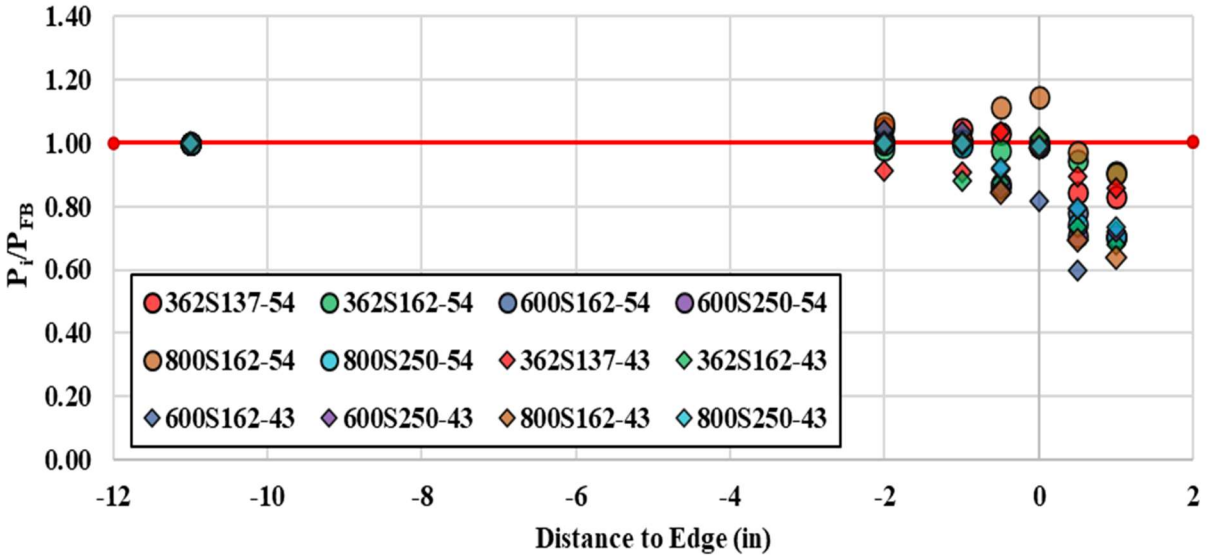

Figure 16: Change in predicted capacities observed in the FEA models (P_i/P_{FB})

5. Comparison with predictive methods

The measured capacities from the FEA analysis were compared with predictions from AISI 100 Chapter E direct strength equations (AISI 2016 and Schafer 2006), AISI S100 Chapter H 2-D interaction equation (Eqn. 1), and theoretical Euler buckling solution (Eqn. 2). All strength calculations were performed with nominal dimensions and material properties as noted in Section 4.1. and the ends were assumed to be simply supported (K=1.0).

$$\frac{\overline{P}}{P_a} + \frac{\overline{M_x}}{M_{ax}} \leq 1.0 \tag{1}$$

$$P_{cr} = \frac{\pi^2 EI}{(KL)^2} \tag{2}$$

In Equation 1, $\bar{P}$ and $\overline{M_x}$ are required strengths ($\overline{M_x} = \bar{P}e_y$, where e_y is the assumed induced eccentricity), P_a is the available axial strength, and M_{ax} is the available flexural strength. These were calculated based on recommendations in AISI S100-16 (AISI 2016) Chapter E and Chapter F respectively. Eccentricities (e_y) for the overhanging specimen for strength calculation were calculated in CUFSM (Schafer and Adany 2006) by neglecting the part of the cross section overhanging from the concrete slab. These values have been reported in Table 3. Equation 2 is the Euler buckling equation where E is the modulus of steel (Taken as 29,500 ksi), I is the moment of inertia about the axis of interest, and L (91 in.) is the length of the column.

Table 3: Calculated eccentricities

Section	e_y (in)		Section	e_y (in)		Section	e_y (in)	
	OH0.5	OH1.0		OH0.5	OH1.0		OH0.5	OH1.0
362S137-43	0.77	0.99	600S162-43	0.97	1.20	800S162-43	1.03	1.27
362S137-54	0.76	0.98	600S162-54	0.96	1.19	800S162-54	1.03	1.26
362S162-43	0.84	1.04	600S250-43	1.15	1.41	800S250-43	1.25	1.53
362S162-54	0.83	1.03	600S250-54	1.14	1.41	800S250-54	1.24	1.53

Comparison of measured (FEA) capacities and capacities predicted by the AISI S100 (AISI 2016) Chapter E (AISI 1-D) and Chapter H interaction equation (AISI 2-D) can be seen in Figure 17.(a) and Figure 17.(b) below. The current AISI Chapter E design equation predicted capacities well at the FB and near edge conditions (E2.0, E1.0, E0.5, E00) but performance dropped to below 1.0 at the OH0.5 and OH1.0 cases as the equation does not consider overhangs. Table 4.(a) summarizes the mean measured to predicted ratios for the 1-D equation at all the bearing conditions. The 2-D interaction equation (Eqn. 1) with assumed eccentricities (Table 3) performed better at the overhangs, improving mean measured to predicted ratio back to above 1.0 (mean $P_{FEA}/P_{AISI\ 2\text{-}D,\ OH0.5}$ = 1.14 & mean $P_{FEA}/P_{AISI\ 2\text{-}D,\ OH1.0}$ = 1.17) for the overhang cases. Euler's equation is unable to account for overhang as well as the reduction due to local buckling interaction with global buckling and has the lowest performance across all the bearing conditions [Table 4.(c)].

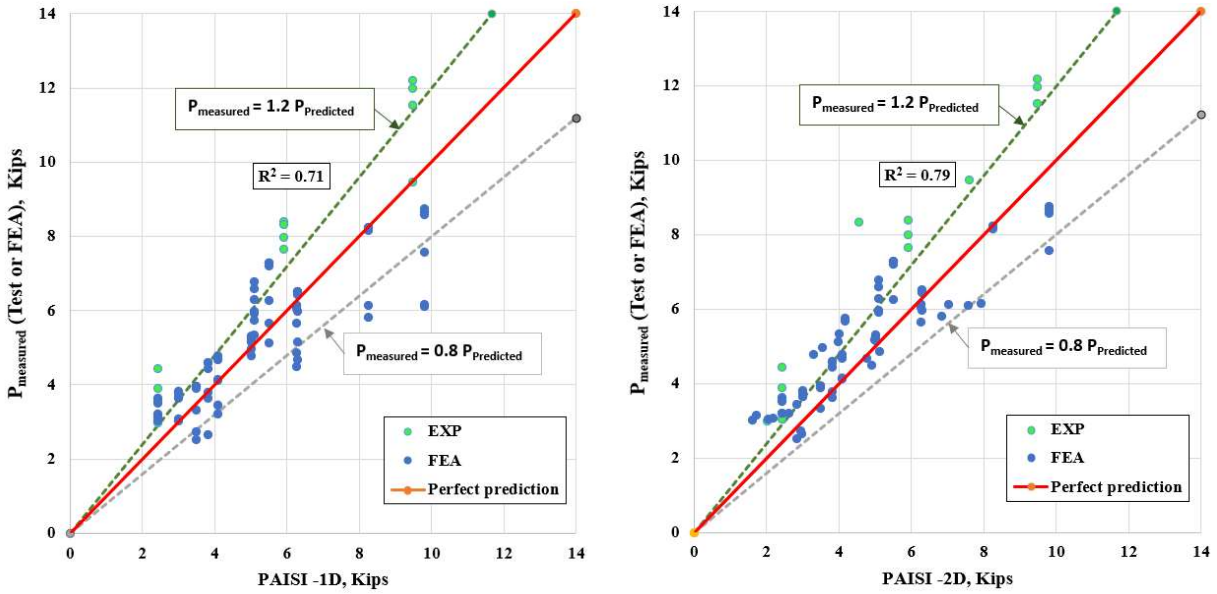

Figure 17: Comparison of measured FEA and experimental strength vs predicted strength: (a) AISI 1-D (b) AISI 2-D

Table 4: Comparison of mean measured strength (FEA) vs prediction: (a) AISI 1-D (b) AISI 2-D (c) Euler

(a) $P_{FEA}/P_{AISI\ -\ 1D}$

	FB	E2.0	E1.0	E0.5	E0.0	OH0.5	OH1.0
Mean	1.10	1.14	1.12	1.06	1.14	0.91	0.79
St. Dev	0.12	0.15	0.14	0.17	0.18	0.22	0.30

(b) $P_{FEA}/P_{AISI\ -\ 2D}$

	FB	E2.0	E1.0	E0.5	E0.0	OH0.5	OH1.0
Mean	1.10	1.14	1.12	1.06	1.14	1.14	1.19
St. Dev	0.12	0.15	0.14	0.17	0.18	0.24	0.31

(c) P_{FEA}/P_{Euler}

	FB	E2.0	E1.0	E0.5	E0.0	OH0.5	OH1.0
Mean	0.72	0.78	0.76	0.68	0.74	0.63	0.55
St. Dev	0.28	0.31	0.29	0.34	0.37	0.31	0.32

8. Conclusions

Based on the results of the numerical and experimental works completed thus far, the following conclusions were drawn –

- A capacity reduction was observed as the specimen was placed over the edge. The average reduction in capacity from the full-bearing case at 0.5 in. and 1.0 in overhang was 0.20 and 0.23 respectively
- AISI 2-D interaction equation performed better at predicting strength and reduction in capacity than 1-D equation and Euler's equation
- Developed FEA model has good agreement with experimental results and modelling methodology is suitable for parametric evaluation
  (Mean test to predicted ratio = 1.02, Standard deviation = 0.14)

9. Future works

The FEA model developed and presented in this paper will be used to expand available data to 66 CFS stud cross sections representing a wide suite of commercially available cross sections from the SSMA Technical Guide (SSMA 2022). This data will be combined with the 1872 configurations already evaluated and presented in Joorabchian et al. (2021) to assess the impact non-uniform bearing conditions have on capacity and stud end stress distribution. The numerical modelling matrix for this FEA expansion can be seen in Table 5 below.

Table 5: Future numerical expansion modelling matrix

Web depth[*1,2]	**Flange width**	**Thicknesses**
(in)	**(in)**	**(mil)**
3.625	1.375, 1.625, &2.000	33, 43, 54, & 68
4.000	1.375, 1.625, &2.000	33, 43, 54, & 68
5.500	1.625	33, 43, 54, & 68
6.000	1.375, 1.625, 2.000, & 2.500	33, 43, 54, 68, & 97
8.000	1.375, 1.625, 2.000, & 2.500	33, 43, 54, 68, & 97

Notes -

1. Bearing Conditions - FB, F, E5.0, E2.0, E1.0, E0.75, E0.5, E0.25, E0.125, E00, OH0.25, OH0.5, OH1.0

2. 66 cross sections x 13 bearing conditions = 858 configurations

Acknowledgments

The writers gratefully acknowledge the financial support provided by the American Iron and Steel Institute (AISI) standards council, and in-kind material donations from Super Stud Building Products, Hilti and Carl Dietrich. The writers also acknowledge the support and contributions of Mark Gauthier, Structural labs manager, Adem Karasu, Post-Doctoral Research Associate, and Elizabeth Hamilton, Undergraduate Researcher, from UMass Amherst to the experimental and numerical works presented herein.

References

ABAQUS (2014). ABAQUS standard version 6.14-4, Dassault Systems Simulia Corp.

AISI (2016). "AISI S100, North America Specification for the Design of Cold-Formed Steel Structures", American Iron and Steel Institute, Washington, D.C.

AISI (2015). "AISI S240, North America Standard for Cold-Formed Steel Structural Framing", American Iron and Steel Institute, Washington, D.C.

A.S. Genikomsou, M.A. Polak, (2015). "Finite element analysis of punching shear of concrete slabs using damaged plasticity model in ABAQUS", *Engineering Structures*, 98, 38–48.

ASTM (2016). "ASTM E8/E8M-16a, Standard Test Methods for Tension Testing of Metallic Materials", ASTM International, West Conshohocken, PA.

ASTM (2018.a). "ASTM C31/C31M-18b, Standard Practice for Making and Curing Concrete Test Specimens in the Field", ASTM International, West Conshohocken, PA.

ASTM (2018.b). "C39/C39M- 18, Standard Test Method for Compressive Strength of Cylinder Concrete Specimens", ASTM International, West Conshohocken, PA.

Bae, S., Belarbi, A, LaBoube, R.A. (2006). Bearing Strength of Slabs on Grade Supporting a Cold-Formed Steel Wall in Low-Rise Building, *Journal of Architectural Engineering*, 12 (1) (2006) 24–32.

Joorabchian, A. (2021). "Cold-Formed Steel Stud Assemblies Bearing on Concrete Slabs (Doctor of Philosophy dissertation)", Civil and Environmental Eng. Department, University of Massachusetts Amherst.

Joorabchian, A, Li, Z, Peterman, K.D. (2021). "Experimental and numerical investigation of fixed-height cold-formed steel wall assemblies bearing on concrete slabs." *Thin-Walled Structures*, 166.

Liao, F., Wu, H., Wang, R., Zhou, T. (2017). "Compression test and analysis of multi-limbs built-up cold-formed steel stub columns", *Journal of Constructional Steel Research*, 128 (2017) 405–415.

Polyzois, D., Fox, S. (2011). "Bearing of Steel Studs on Concrete", Newsletter for the Light Gauge Steel Engineering Association (now the Cold-Formed Steel Engineering Institute).

Schafer, B. W., Li, Z., Moen, C. D. (2010). "Computational modeling of cold-formed steel." *Thin-Walled Structures*, 48(10-11), 752–762.

Schafer, B.W., Ádány, S. (2006). "Buckling analysis of cold-formed steel members using CUFSM: Conventional and constrained finite strip method", *Proceedings of 18th International Specialty Conference on Cold-Formed Steel Structures*, Orlando, FL

Schafer, B.W. (2006). "Direct Strength Method (DSM) Design Guide", American Iron and Steel Institute, Washington, D.C.

SSMA (2022). "Product technical guide", Steel Stud Manufacturers Association, Boise, ID.

Zeinoddini, V. M., Schafer, B. W. (2012). "Simulation of geometric imperfections in cold-formed steel members using spectral representation approach." *Thin-Walled Structures*, 60, 105–117